Chinese Chemical Letters 32 (2021) 2243–2248

Contents lists available at ScienceDirect

Chinese Chemical Letters

journal homepage: www.elsevier.com/locate/cclet

Communication

Designed preparation of CoS/Co/MoC nanoparticles incorporated in N and S dual-doped porous carbon nanofibers for high-performance Zn-air batteries

Yanrong Ren[a,1], Haiyan Wang[a,1], Tianyu Zhang[b,1], Luankexin Ma[c], Pengcheng Ye[a], Yijun Zhong[a], Yong Hu[a,*]

[a] Key Laboratory of the Ministry of Education for Advanced Catalysis Materials, Department of Chemistry, Zhejiang Normal University, Jinhua 321004, China
[b] School of Biological and Medical Engineering, School of Food Science and Engineering, Hefei University of Technology, Hefei 230009, China
[c] Queen Mary University of London Engineering School, NPU/Material Science and Engineering, Northwestern Polytechnical University, Xi'an 710000, China

ARTICLE INFO

Article history:
Received 17 November 2020
Received in revised form 22 December 2020
Accepted 23 December 2020
Available online 31 December 2020

Keywords:
CoS
Co
MoC
Porous carbon nanofibers
Zn-air batteries

ABSTRACT

The development of low-cost and highly efficient bifunctional electrocatalysts toward oxygen reduction reaction (ORR) and oxygen evolution reaction (OER) is of critical importance for clean energy devices such as fuel cells and metal-air batteries. Herein, a sophisticated nanostructure composed of CoS, Co and MoC nanoparticles incorporated in N and S dual-doped porous carbon nanofibers (CoS/Co/MoC-N, S-PCNFs) as a high-efficiency bifunctional electrocatalyst is designed and synthesized *via* an efficient multi-step strategy. The as-prepared CoS/Co/MoC-N, S-PCNFs exhibit a positive half-wave potential ($E_{1/2}$) of 0.871 V for ORR and a low overpotential of 289 mV at 10 mA/cm^2 for OER, outperforming the non-noble metal-based catalysts reported. Furthermore, the assembled Zn-air battery based on CoS/Co/MoC-N, S-PCNFs delivers an excellent power density (169.1 mW/cm^2), a large specific capacity (819.3 mAh/g) and robust durability, demonstrating the great potential of the as-developed bifunctional electrocatalyst in practical applications. This work is expected to inspire the design of advanced bifunctional nonprecious metal-based electrocatalysts for energy storage.

With the energy crisis and environmental pollution question gradually intensifies, the demand for clean energy has stimulated great efforts to develop highly efficient storage and conversion equipment [1–3]. Among various candidates, rechargeable Zn-air batteries featuring low cost, environmental friendliness and excellent theoretical energy density (1086 Wh/kg) characteristics have been considered one of the most promising devices [4–6]. However, the rechargeable Zn-air batteries are still suffering from unsatisfactory electrochemical performance, such as limited output power density, large overpotential, and poor charge-discharge stability, which are mainly impeded by the sluggish kinetics and the electrochemical stability during oxygen reduction reaction (ORR) and oxygen evolution reaction (OER) processes [7–9].

Although the benchmark catalysts such as Pt, RuO_2 and IrO_2 have shown outstanding activities for ORR and OER, some critical problems including the scarcity, high price and inferior durability still restrict their widespread applications [10–13]. Besides, most catalysts have been designed for a particular reaction so far [14–16]. The preparation of two separate electrodes requires different materials and complicated processes, thus increasing the preparation cost and the complexity of the equipment. In this regard, combining these two catalytic functions into an integrated electrode has practical appeal. The design of bifunctional catalysts not only simplifies the structure of the unit, but also gives a unique explanation of the interaction between active species and reaction intermediates [17–19]. Hence, it is urgent but still a challenge to realize multiple active sites in one system, and explore high performance and practical non-noble metal bifunctional electrocatalysts toward both ORR and OER.

Metal-organic frameworks (MOFs) assembled from transition metal sources and organic ligands, offer a rich platform for functionally tailoring nanoporous transition metal/heteroatom-doped carbon materials. The obtained materials often possess high surface areas, large porosities and abundant active sites, thereby showing excellent electrocatalytic activities [20–23]. Moreover, the MOF-derived materials can be designed in different ways by combing metallic species toward bifunctional or multifunctional

* Corresponding author.
E-mail address: yonghu@zjnu.edu.cn (Y. Hu).
[1] These authors contributed equally to this work.

https://doi.org/10.1016/j.cclet.2020.12.050

applications. While for the sake of improving the stability of MOF-derived catalysts, the researchers have proposed a method of encapsulate transition metal nanoparticles in porous carbon shell for electrocatalysis [24]. It is worth noting that 1D carbon materials type, such as carbon nanofibers and carbon nanotubes, possess high electric conductivity, long electron channels and high aspect ratios, which can provide easy channels for O_2 diffusion and contribute to exposure more active reaction sites [25–27]. Furthermore, the introducing of heteroatoms into carbon nanofibers not only improves their electrical conductivity, but also povides additional active sites for ORR and OER [28–30]. The electronic properties of metal core and carbon shell can also be efficiently tuned with the introduction of heteroatoms to improve the electrocatalytic performance. For instance, Xia *et al.* presented the tin disulfide (SnS_2) inserteded in nitrogen and sulfur co-doped carbon (SnS_2/NSDC) exhibited excellent electrochemical properties [31]. Electrospinning is a simple method to synthesis uniform fibers with large specific surface area and superior stability [32,33], which provides an efficient method to synthesis of advanced MOFs-derived metal nanoparticles incorporated in heteroatom-doped carbon nanofibers catalysts toward ORR and OER.

Inspired by the foregoing, we designed an efficient and stable bifunctional CoS, Co and MoC nanoparticles incorporated in the N, S dual-doped porous carbon nanofibers (CoS/Co/MoC-N, S-PCNFs) catalyst by a multi-step approach. In this feasible design, cobalt-based zeolitic imidazolate framework encapsulated in polyacrylonitrile nanofibers (ZIF-67@PAN NFs) were first prepared by electrospinning ZIF-67 into 1D nanofibers, which could protect the metal from agglomeration at high temperature. The obtained product was subsequently etched with $(NH_4)_2MoS_4$ to produce a porous structure and introduce Mo and S sources, and finally pyrolyzed at high temperature under N_2 atmosphere to obtain CoS/Co/MoC-N, S-PCNFs. Benefiting from the purposely designed 1 D nanofiber morphology, high surface area, nanoparticles incorporated in carbon nanofibers structure, and the integration of multiple active sites including CoS, Co and MoC, the as-prepared CoS/Co/MoC-N, S-PCNFs catalyst, ORR showed a positive half-wave potential ($E_{1/2}$ = 0.871 V) and OER showed a low overpotential (289 mV) at 10 mA/cm^2, outperforming the most repored non-noble metal-based component catalysts. Specifically, CoS/Co/MoC-N, S-PCNFs also showed a low voltage gap ($E_{j\ =\ 10\ (OER)}$ - $E_{1/2\ (ORR)}$ = 0.648 V), which endows Zn-air batteries with excellent performance. A high-power density (169.1 mW/cm^2), a large specific capacity (819.3 mAh/g), a remarkable energy density (1008.1 Wh/kg) and superior cycling durability were achieved with the as-assembled rechargeable Zn-air battery based on CoS/Co/MoC-N, S-PCNFs, which provided a further evidence of the feasibility and advantages of the bi-functional electrocatalyst for energy storage. Efficient CoS/Co/MoC-N, S-PCNFs bifunctional oxygen electrocatalyst was designed and synthesized *via* a facile multi-step strategy.

Synthesis of ZIF-67: 0.87 g of $Co(NO_3)_2{\cdot}6H_2O$ and 1.97 g of 2-methylimidazole (2-MIM) were sonicated in 70 mL of methanol to obtain solution A and B, respectively. Then solution A was poured into solution B for 5 min under stirring. The mixed solution was aged at atmospheric room temperature for 1 h. The product was obtained collected by centrifugation and washed with methanol and ethanol in turn.

Synthesis of ZIF-67@PAN NFs: 0.25 g of ZIF-67 was dispersed into 4.5 mL of *N*,*N*-dimethylformamide (DMF) under ultrasonic for 1 h, followed by the addition of 0.5 g of polyacrylonitrile (PAN) (M_w = 150,000 g/mol) under vigorous stirring at ambient temperature for 10 h to form a homogeneous solution. Then, the homogeneous solution was transferred into a plastic syringe with a 21-gauge tip stainless-steel needle that was connected to a high voltage of 13 kV. The ZIF-67@PAN NFs ejected from the needle were collected with aluminum foil (30 × 20 cm^2) and dried at 80 °C for 12 h in a vacuum oven.

Synthesis of CoS/Co/MoC-N, S-PCNFs: First, 5 mL of aqueous solution containing 20 mg of $(NH_4)_2MoS_4$ was uniformly mixed with 20 mL of methanol. Subsequently, 160 mg of ZIF-67@PAN NFs was added into the above solution. After stirring for 1 h, the obtained product was washed with ethanol several times and then dried in oven at 60 °C. Finally, the as-obtained product was annealed at 800 °C under N_2 atmosphere for 2 h with a ramp rate of 5 °C/min. Then the tube furnace was naturally cooled to ambient temperature, the resulting black powder was obtained and named CoS/Co/MoC-N, S-PCNFs-20. CoS/Co/MoC-N, S-PCNFs-10 and CoS/Co/MoC-N, S-PCNFs-40 were obtained with the same procedure to that of CoS/Co/MoC-N, S-PCNFs-20, but ZIF-67@PAN NFs were etched with the solutions containing 10 mg and 40 mg of $(NH_4)_2MoS_4$, respectively.

Synthesis of Co-N-PCNFs: Co nanoparticles incorporated in N-doped porous carbon nanofibers (Co-N-PCNFs) were obtained with the same procedure to that of CoS/Co/MoC-N, S-PCNFs-20, but ZIF-67@PAN NFs were not etched with $(NH_4)_2MoS_4$.

The detailed procedure of materials characterization, electrochemical measurements and the assembly process of Zn-air battery can be seen in the Supporting information.

The synthetic process of the CoS/Co/MoC-N, S-PCNFs sample involves four steps, as illustrated in Fig. 1a. SEM image shows that the synthesis starts from the organometallic reaction of Co^{2+} and 2-MIM to form ZIF-67 which exhibits a polyhedron morphology (Fig. 1b). Subsequently, the as-prepared ZIF-67 was encapsulated in PAN nanofibers by electrospinning method to form ZIF-67@PAN NFs. Fig. 1c shows the 1D fiber structure of ZIF-67@PAN NFs with an average diameter of 1 μm and a rough surface. The X-ray

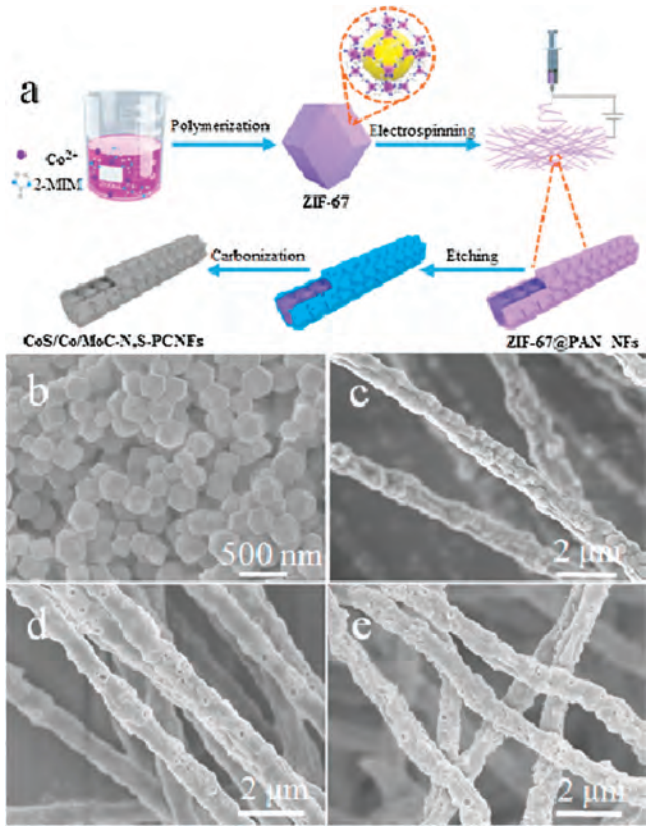

Fig. 1. (a) Schematic illustration of the preparation of the CoS/Co/MoC-N, S-PCNFs. SEM images of the as-prepared (b) ZIF-67, (c) ZIF-67@PAN NFs, (d) ZIF-67@PAN NFs after etching with 20 mg $(NH_4)_2MoS_4$, and (e) CoS/Co/MoC-N, S-PCNFs-20.

diffraction (XRD) pattern of ZIF-67@PAN NFs matches well with the characteristic peaks of ZIF-67 (Fig. S1 in Supporting information), demonstrating ZIF-67 were entirely embedded in PAN nanofibers [34,35]. Then the as-prepared ZIF-67@PAN NFs were immersed in $(NH_4)_2MoS_4$ solution for further ion etching treatment. The possible mechanism is that MoS_4^{2-} penetrates through the fiber to combine with Co^{2+} ions that released from the ZIF to form Co-MoS_4 [36]. The surface of these fibers after etching becomes porous, as displayed in Fig. 1d. After subjection to high temperature under N_2 atmosphere, the 1D nanofibers shape is preserved, whereas the surface of CoS/Co/MoC-N, S-PCNFs becomes rougher and the average diameter of the carbon fiber is reduced to about 900 nm, which may be caused by the shrinkage of the polymer during carbonization (Fig. 1e). To explore the effect of $(NH_4)_2MoS_4$, the as-prepared ZIF-67@PAN NFs were etched with 0, 10, 20 and 40 mg of $(NH_4)_2MoS_4$ to prepare Co-N-PCNFs and different CoS/Co/MoC-N, S-PCNFs samples (CoS/Co/MoC-N, S-PCNFs-10, CoS/Co/MoC-N, S-PCNFs-20, CoS/Co/MoC-N, S-PCNFs-40), respectively. The samples all maintain the 1D nanofiber structure (Figs. S2 and S3 in Supporting information). The energy dispersive X-ray spectroscopy (EDX) spectra (Fig. S4 in Supporting information) confirms that Mo and S are not existed in Co-N-PCNFs. In addition, the percent contents of Mo and S in CoS/Co/MoC-N, S-PCNFs increase with the addition amount of $(NH_4)_2MoS_4$. The Co/Mo atomic ratio is about 9.5 for CoS/Co/MoC- N, S-PCNFs-20.

Transmission electron microscopy (TEM) was further employed to investigate the microstructure of the as-obtained CoS/Co/MoC-N, S-PCNFs catalyst. Fig. 2a clearly shows that numerous small nanoparticles are uniformly incorporated in nanofibers. The high-resolution TEM (HRTEM) image in Fig. 2b shows lattice fringe of 0.21 nm corresponding to the (111) plane of Co, and lattice spacings of 0.19 nm and 0.12 nm are assigned to CoS (102) and MoC (200), respectively. The existence of Co, CoS and MoC is further proved in the selected area electron diffraction (SAED) (Fig. 2c). Moreover, the TEM elemental mapping represented a homodisperse of Co, Mo, S, N and C throughout the whole carbon nanofibers (Figs. 2d-i).

The XRD patterns of the Co-N-PCNFs, CoS/Co/MoC-N, S-PCNFs-10, CoS/Co/MoC-N, S-PCNFs-20 and CoS/Co/MoC-N, S-PCNFs-40 are shown in Fig. 3a and Fig. S5 (Supporting information). Diffraction peaks at 44.0°, 51.7° and 76.0° are assigned to Co (JCPDS No. 15-0806) and the peak at around 25° could be indexed to (002) plane of graphitic carbon [37]. Besides, those peaks located at 32.2°, 35.8°, 48.8°, 64.3° and 78.5° are ascribed to MoC (JCPDS No.45–1015) and the peak intensity of MoC increases with the amount of $(NH_4)_2MoS_4$ [38]. The disappearance of the characteristic peaks for CoS may be attributed to its low crystallinity. Further to identify the existence of CoS, Raman spectra dates were collected. The peaks at 187, 472, 513 and 676 cm^{-1} for the CoS/Co/MoC-N, S-PCNFs samples belong to the A_g, E_g, F_{2g} and A_{1g} peaks of CoS, respectively (Fig. 3b and Fig. S6 in Supporting information), whereas these peaks are not found in the Raman spectrum of the Co-N-PCNFs [39,40]. The characteristic peaks around 1350 and 1580 cm^{-1} originate from D and G band, respectively, and the I_D/I_G ratio of CoS/Co/MoC-N, S-PCNFs-20 is 1.04, which is higher than Co-N-PCNFs (0.93), implying more structural defects. Moreover, as the amount of $(NH_4)_2MoS_4$ increases, the I_D/I_G value of the sample increases, indicating an enhanced defect degree.

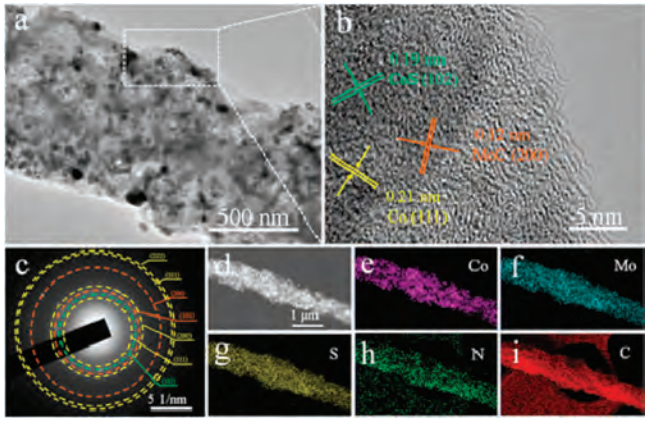

Fig. 2. (a) TEM image, (b) HRTEM image, (c) SAED pattern and (d) STEM image of the as-prepared CoS/Co/MoC-N, S-PCNFs-20. (e-i) Corresponding elemental mapping.

To gain further investigate the chemical composition of the as-prepared catalysts, X-ray photoelectron spectroscopy (XPS) was conducted. Fig. 3c shows the co-existence of Co, Mo, S, N, C and O elements in CoS/Co/MoC-N, S-PCNFs-20, whereas Co-N-PCNFs only contain Co, N, C and O elements (Fig. S7a and Table S1 in Supporting information). The Co 2p spectra of CoS/Co/MoC-N, S-PCNFs-20 shows the main peaks of metallic Co (778.5 and 793.4 eV), Co-S (778.9 and 794.5 eV), Co $2p_{1/2}$ (781.3 eV) and Co $2p_{3/2}$ (797.3 eV) with a pair of satellites peaks at 785.5 and 802.5 eV (Fig. 3d), while the peaks for Co-S are not found in the Co 2p XPS spectrum of Co-N-PCNFs (Fig. S7b in Supporting information) [41–45]. The two peaks centered at 228.8 and 232.2 eV in the Mo 3d XPS spectrum are assigned to Mo^{4+} and the peak at 235.4 eV corresponds to Mo^{6+} (Fig. 3e) [46,47]. The surface oxidation of molybdenum carbide nanoparticles in air may be the cause of high-valence Mo [48]. The S $2p_{1/2}$ and S $2p_{3/2}$ peaks for CoS/Co/MoC-N, S-PCNFs-20 located at 163.4 and 162.1 eV correspond to S^{2-} (Fig. 3f). Moreover, the peak at 164.4 eV is assigned to C—S—C bond [49–51]. The N 1s spectra can be deconvoluted to five peaks, corresponding to the Mo 3p (395.0 eV) and four different types of N species including pyridinic N (398.3 eV), Co-N (399.4 eV), pyrrolic N (400.1 eV), and graphitic N (401.5 eV) (Fig. 3g and Fig. S7c in Supporting information) [52–54]. The atomic percentages of different N types be provided in Table S2 (Supporting information). The C 1s XPS spectrum provides evidence that S and N are indeed doped into the carbon matrix of CoS/Co/MoC-N, S-PCNFs-20 is also proved by the C 1s XPS spectrum, while only N element is doped in Co-N-PCNFs (Fig. 3h and Fig. S7d in Supporting information) [55,56]. We can conclude from the above test results that CoS/Co/MoC-N, S-PCNFs-20 contain CoS, Co, MoC and N, S dual-doped porous carbon nanofibers, while metallic Co and N-doped porous carbon nanofibers exist in Co-N-PCNFs.

Nitrogen adsorption-desorption experiment was further used to explore the porous structure of CoS/Co/MoC-N, S-PCNFs-20 and Co-N-PCNFs. The two catalysts exhibit the typical type IV profiles with distinct hysteresis loops (Fig. 3i), indicating the existence of abundant micropores and mesopores [57]. The pore size distribution curves in Fig. S8 (Supporting information) also confirm that the samples possess a hierarchical pore structure containing micro- and mesopores, which are in accordance with the results obtained from SEM images. Besides, the specific surface area of CoS/Co/MoC-N, S-PCNFs-20 is 312 m^2/g which is higher than 149 m^2/g for Co-N-PCNFs. The hierarchical pore structure containing micro- and mesopores, and high specific surface area of CoS/Co/MoC-N, S-PCNFs-20 are beneficial to the exposure of active sites and the fast ion transfer, thus facilitating the electrochemical reactions.

The ORR performance of the as-prepared catalysts was further investigated in 0.1 mol/L KOH solution. The cyclic voltammetry (CV) curves of CoS/Co/MoC-N, S-PCNFs-20 in the O_2 and N_2-saturated electrolyte were compared in Fig. S9 (Supporting information). A significant cathodic peak at 0.81 V is found in O_2-saturated electrolyte, manifesting the ORR activity of CoS/Co/MoC-N, S-PCNFs-20. The ORR activity of the as-prepared catalysts

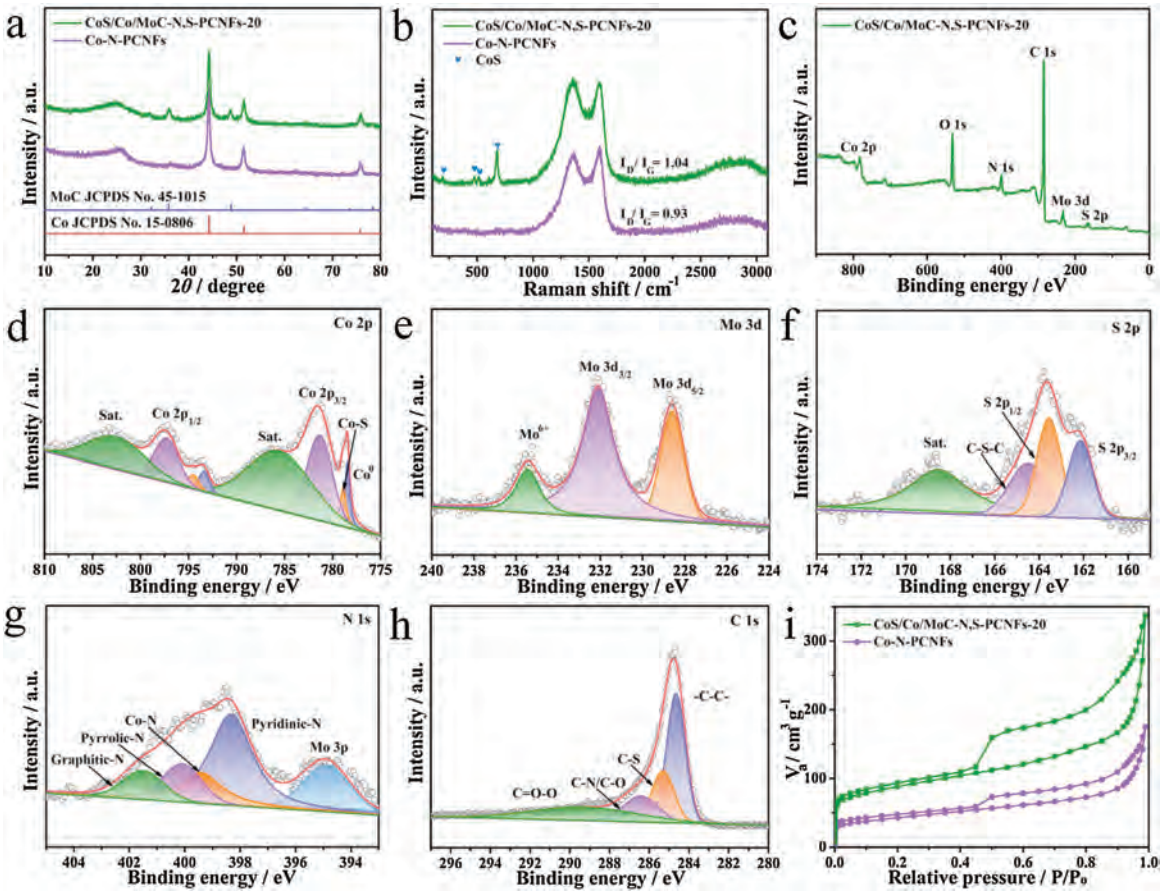

Fig. 3. (a) XRD patterns and (b) Raman spectra of CoS/Co/MoC-N, S-PCNFs-20 and Co-N-PCNFs. (c) XPS survey spectrum of CoS/Co/MoC-N, S-PCNFs-20. High-resolution (d) Co 2p, (e) Mo 3d, (f) S 2p, (g) N 1s and (h) C 1s XPS spectra of the CoS/Co/MoC-N, S-PCNFS-20. (i) Nitrogen adsorption-desorption isotherm curves of the CoS/Co/MoC-N, S-PCNFs-20 and Co-N-PCNFs.

was then evaluated by linear sweep voltammetry (LSV) on a rotating disk electrode (RDE) at a rotation rate of 1600 rpm. As shown in Fig. 4a, CoS/Co/MoC-N, S-PCNFs-20 exhibit the best ORR activity with an onset potential (E_0) of 0.951 V and $E_{1/2}$ of 0.871 V, which are higher than those of Co-N-PCNFs (E_0 = 0.949 V, $E_{1/2}$ = 0.856 V) and Pt/C (E_0 = 0.940 V, $E_{1/2}$ = 0.840 V). Besides, the E_0 and $E_{1/2}$ of CoS/Co/MoC-N, S-PCNFs-20 is comparable to the other CoS/Co/MoC-N, S-PCNFs catalysts (Fig. S10a in Supporting information) and also surpasses most reported precious-metal-free electrocatalysts (Table S3 in Supporting information). Moreover, the Tafel slope of CoS/Co/MoC-N, S-PCNFs-20 was the lowest (86.8 mV/dec) among all the catalysts, signifying a more favorable ORR kinetics (Fig. S10b and Fig. S11 in Supporting information). The kinetic parameters for n are further analyzed by the LSV curves at variable rotation rates (Fig. S12a in Supporting information). The corresponding Koutecky-Levich (K–L) curves show a good linearity with the growing potential and the calculated electron transfer number (n) is 3.9 for CoS/Co/MoC-N, S-PCNFs-20, indicating a four electron ORR progress (Fig. S12b in Supporting information). The n value is also accessed by the rotating ring disk electrode (RRDE) measurement. The yield of H_2O_2 is less than 4% and the corresponding n is 3.98 which is in accordance with the result of K–L plot, further verifying excellent $4e^-$ pathway selectivity of CoS/Co/MoC-N, S-PCNFs-20 catalyst (Fig. S13 in Supporting information). Besides catalytic activity, the stability is a critical parameter for evaluating the practically of catalysts. As presented in Fig. 4b, CoS/Co/MoC-N, S-PCNFs-20 preserves 93% of current density after a continuous operation for 36,000 s, while Pt/C suffers from a conspicuous degradation with only 42% retention, indicating a better durability of CoS/Co/MoC-N, S-PCNFs-20 over Pt/C catalyst.

Furthermore, the OER performance is further measured in 1.0 mol/L KOH solution. CoS/Co/MoC-N, S-PCNFs-20 displays a lower overpotential of 289 mV, in comparison to the other samples at a current density of 10 mA/cm^2 (Fig. 4c and Fig. S14a in Supporting information). These values are comparable to the state-of-the-art OER catalysts that have been reported (Table S4 in Supporting information). Additionally, the outstanding Tafel slope of CoS/Co/MoC-N, S-PCNFs-20 (117.9 mV/dec) is compared with other samples (Figs. S14b and S15 in Supporting information), indicating profitably OER kinetics. The electrochemical impedance spectroscopy (EIS) test result consists well with Tafel that the charge transfer resistance (R_{ct}) of CoS/Co/MoC-N, S-PCNFs-20 is the smallest (Fig. S16 and Table S5 in Supporting information). Moreover, as shown in Fig. S17 (Supporting information), CoS/Co/MoC-N, S-PCNFs-20 also show excellent long-term operation durability for 45 h. The polarization curves of the CoS/Co/MoC-N, S-PCNFs-20 shows a negligible decrease after a long-term OER and ORR stability test compared to its pristine counterpart (Fig. S18 in Supporting information), indicating the good stability of CoS/Co/MoC-N, S-PCNFs-20. To further prove the excellent bifunctional activities of the catalyst, the overall activities of CoS/Co/MoC-N, S-PCNFs-20 for OER and $E_{1/2}$ for ORRwas measured by $\Delta E = E_{j = 10\,(OER)} - E_{1/2\,(ORR)}$. The ΔE value obtained for the CoS/Co/MoC-N, S-PCNFs-20 is 0.648 V, which is considerably smaller than the comparative catalysts (Fig. S19a in Supporting information). Moreover, the overvoltage gap of CoS/Co/MoC-N, S-PCNFs-20 is even lower than those values of other reported excellent bifunctional catalysts

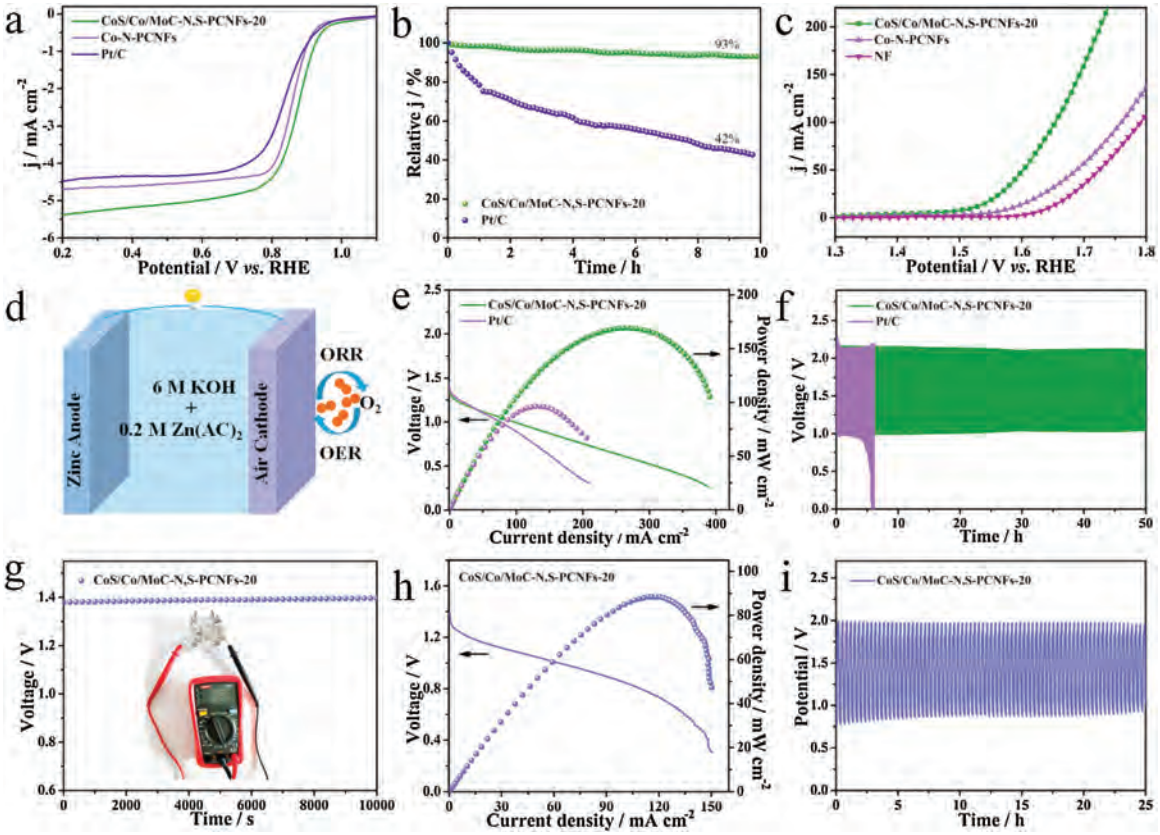

Fig. 4. The ORR and OER performance of the CoS/Co/MoC-N, S-PCNFs-20, Co-N-PCNFs and Pt/C or NF catalysts: (a) ORR LSV curves with a rotating speed of 1600 rpm. (b) Chronoamperometric curves of the CoS/Co/MoC-N, S-PCNFs-20, compared with commercial Pt/C. (c) OER LSV curves, with iR corrected. (d) Schematic illustration of the liquid rechargeable Zn-air battery configuration. (e) Discharge polarization curves and power density plots of the CoS/Co/MoC-N, S-PCNFs-20 and Pt/C catalysts. (f) Cycling stability of CoS/Co/MoC-N, S-PCNFs-20 and Pt/C catalysts. (g) Open circuit plot with an inset of a photograph of the solid Zn-air battery (h) Discharge polarization curves and the power density plots of CoS/Co/MoC-N, S-PCNFs-20. (i) Galvanostatic cycling stability of CoS/Co/MoC-N, S-PCNFs-20 at a current density of 2 mA/cm^2.

(Fig. S19b and Table S6 in Supporting information), demonstrating the superiority of the bifunctional CoS/Co/MoC-N, S-PCNFs-20 catalyst. We can speculate that the better electrocatalytic activity of CoS/Co/MoC-N, S-PCNFs-20 than that of Co-N-PCNFs may because CoS, Co and MoC all play important roles on the final bifunctional performance.

In order to investigate the active roles of CoS, Co and MoC as well as their synergistic effect, Co and CoS species exposed in CoS/Co/MoC-N, S-PCNFs-20 can be removed by HCl etching experiment. The morphology and phase of the CoS/Co/MoC-N, S-PCNFs-20 after acid etching have no obvious change, demonstrating a good stability (Figs. S20 and S21 in Supporting information). The intensity of diffraction peaks for metallic Co decreases significantly, signifying a large amount of Co nanoparticles are removed. In addition, the characteristic peaks of CoS also show similar trend in the Raman spectrum of CoS/Co/MoC-N, S-PCNFs-20 after acid etching, demonstrating CoS nanoparticles were removed a lot (Fig. S22 in Supporting information). After acid etching, the ORR and OER performance of CoS/Co/MoC-N, S-PCNFs-20 declines obviously, indicating metallic Co and CoS are both beneficial for ORR and OER (Fig. S23 in Supporting information). Electrochemical surface area (ECSA) of the samples were then assessed by the electrochemical double-layer capacitance (C_{dl}) to show the inherent activity. The CV curves of CoS/Co/MoC-N, S-PCNFs and Co-N-PCNFs samples at various scan rates of 10, 20, 40, 60, 80 and 100 mV/s (Fig. S24 in Supporting information). As expected, CoS/Co/MoC-N, S-PCNFs-20 has larger C_{dl} of 62.9 mF/cm^2 in comparison with Co-N-PCNFs (9.5 mF/cm^2), CoS/Co/MoC-N, S-PCNFs-10 (27.0 mF/cm^2) and CoS/Co/MoC-N, S-PCNFs-40 (36.4 mF/cm^2), indicating the largest ECSA of CoS/Co/MoC-N, S-PCNFs-20 among the four samples (Fig. S25 in Supporting information). The ECSA of the CoS/Co/MoC-N, S-PCNFs-20 after acid etching and the corresponding specific activities normalized by ECSA are presented in Fig. S26 (Supporting information). The large ECSA of CoS/Co/MoC-N, S-PCNFs-20 manifests that more available active sites can be exposed to the electrolyte for accelerating the electrocatalytic reaction. Thus, the superior bifunctional performance of CoS/Co/MoC-N, S-PCNFs-20 toward ORR and OER should originate from the multiple active species of CoS, Co and MoC, and the large ECSA, which can provide plentiful active sites for electrocatalytic reactions.

To demonstrate the practical potential of CoS/Co/MoC-N, S-PCNFs-20 for Zn-air batteries, a liquid rechargeable Zn-air battery is assembled. Fig. 4d shows the schematic diagram of the liquid rechargeable Zn-air battery, which uses carbon fiber paper coated with CoS/Co/MoC-N, S-PCNFs-20 as a cathode electrode, a Zn plate as an anode, and 6 mol/L KOH contains 0.2 mol/L $Zn(AC)_2$ as electrolyte. The size of the Zn cathode was about 1.0 cm^2. The Zn-air cell based on CoS/Co/MoC-N, S-PCNFs-20 delivered the open-circuit voltage of 1.45 V (Fig. S27 in Supporting information). Besides, the voltage still remains stable at around 1.45 V after 10 h. Fig. S28 (Supporting information) compares the charge-discharge curves of the CoS/Co/MoC-N, S-PCNFs-20 and Pt/C-based air electrodes. As presented in Fig. 4e, the power density of CoS/Co/MoC-N, S-PCNFs-20 based Zn-air battery reaches 169.1 mW/cm^2, comparable to Pt/C and other reported catalysts for Zn-air batteries (Table S7 in Supporting information). Fig. S29 (Supporting information) shows the stable galvanostatic discharge curves of

CoS/Co/MoC-N, S-PCNFs-20-based catalyst. The battery exhibits large specific capacities of 819.3 mAh/g and 785.1 mAh/g at discharging current density of 5 mA/cm^2 and 10 mA/cm^2 (normalized by the total mass of consumed Zn), respectively, corresponding to high energy densities of 1008.2 and 907.7 Wh/kg. When CoS/Co/MoC-N, S-PCNFs-20 cathode was discharged at 2, 5, 10, 20, 30 and 40 mA/cm^2, the stable voltage curves verify its outstanding stability (Fig. S30 in Supporting information). In addition, the voltage almost shows no drop during the 50 h charging-discharging test, whereas the Pt/C battery suffers a fast decline after 6 h continuous operation, indicating the superior stability of CoS/Co/MoC-N, S-PCNFs-20 (Fig. 4f).

Finally, all-solid-state Zn-air battery was packaged with CoS/Co/MoC-N, S-PCNFs-20 (Fig. S31 in Supporting information). As demonstrated in Figs. 4g and h, the CoS/Co/MoC-N, S-PCNFs-20-based exhibit open circuit voltage of 1.38 V and power density of 88.4 mW/cm^2, which are outperforming than the advanced carbon-based nanomaterials as the electrocatalysts reported so far (Table S8 in Supporting information). As shown in Fig. 4i, the charging and discharging voltages maintain stable for 25 h at a constant current density of 2 mA/cm^2 by galvanostatic discharge-charges tests, demonstrating the robust rechargeability of CoS/Co/MoC-N, S-PCNFs-20. Moreover, a red light-emitting diodes (LED) screen can be lighteded by two solid-state cells (Fig. S32 in Supporting information). These results all confirmed the great potential of the bifunctional CoS/Co/MoC-N, S-PCNFs-20 catalyst.

In summary, we have developed an efficient bifunctional CoS/Co/MoC-N, S-PCNFs catalyst by a multi-step approach involving polymerization, electrospinning, etching and high-temperature calcination. Benefiting from the advantages of the purposely designed 1D nanofiber morphology, high surface area, nanoparticles incorporated in carbon nanofiber structure, and the integration of multiple active sites including CoS, Co and MoC, the as-prepared CoS/Co/MoC-N, S-PCNFs catalyst demonstrates excellent electrocatalytic performance toward the ORR and OER. High values of E_0 (0.951 V) and $E_{1/2}$ (0.871 V) have been achieved, which outperform those of commercial Pt/C catalyst. Moreover, a lower ΔE value (0.648 V) of CoS/Co/MoC-N, S-PCNFs enables excellent activities including a high-power density (169.1 mW/cm^2), a large specific capacity (819.3 mAh/g) and a remarkable energy density (1008.1 Wh/kg). Also, the as-assembled rechargeable Zn-air battery with CoS/Co/MoC-N, S-PCNFs displays superior cycling stability than that based on Pt/C electrode. This work provides a simple and feasible strategy for preparation of efficient non-noble metal bifunctional electrocatalysts for energy storage.

Declaration of competing interest

The authors declare that they have no known competing financial interests or personal relationships that could have appeared to influence the work reported in this paper.

Acknowledgments

Y. Hu acknowledges the financial support from Natural Science Foundation of China (No. 21671173), the Independent Designing Scientific Research Project of Zhejiang Normal University (No. 2020ZS03) and Zhejiang Provincial Ten Thousand Talent Program (No. 2017R52043).

Appendix A. Supplementary data

Supplementary material related to this article can be found, in the online version, at doi:https://doi.org/10.1016/j.cclet.2020.12.050.

References

[1] C.L. Bentley, M. Kang, P.R. Unwin, J. Am. Chem. Soc. 141 (2019) 2179–2193.
[2] W. Li, J. Liu, D. Zhao, Nat. Rev. Mater. 1 (2016) 16023.
[3] Z. Liu, Z. Zhao, B. Peng, X. Duan, Y. Huang, J. Am. Chem. Soc. 142 (2020) 17812–17827.
[4] Z. Pei, H. Li, Y. Huang, et al., Energy Environ. Sci. 10 (2017) 742–749.
[5] P. Tan, B. Chen, H. Xu, et al., Appl. Catal. B 241 (2019) 104–112.
[6] F. Meng, H. Zhong, D. Bao, J. Yan, X. Zhang, J. Am. Chem. Soc. 138 (2016) 10226–10231.
[7] J. Zhang, L. Dai, Angew. Chem. Int. Ed. 55 (2016) 13296–13300.
[8] J.C. Li, P.X. Hou, S.Y. Zhao, et al., Energy Environ. Sci. 9 (2016) 3079–3084.
[9] G. Fang, J. Gao, J. Lv, et al., Appl. Catal. B 268 (2020) 118431.
[10] S. You, X. Gong, W. Wang, et al., Adv. Energy Mater. 6 (2016) 1501497.
[11] S. Ci, S. Mao, Y. Hou, et al., J. Mater. Chem. A 3 (2015) 7986–7993.
[12] B.Y. Xia, Y. Yan, N. Li, et al., Nat. Energy 1 (2016) 15006.
[13] L. Jin, H. Pang, Chin. Chem. Lett. 31 (2020) 2300–2304.
[14] J. Saha, S. Verma, R. Ball, C. Subramaniam, R. Murugavel, Small 16 (2020) 1903334.
[15] G. Saianand, A.I. Gopalan, J.C. Lee, et al., Small 16 (2020) 1903937.
[16] G. Yuan, S. Yu, J. Jie, et al., Chin. Chem. Lett. 31 (2020) 1941–1945.
[17] Y. Xu, P. Deng, G. Chen, et al., Adv. Funct. Mater. 30 (2020) 1906081.
[18] C.C. Yang, S.F. Zai, Y.T. Zhou, L. Du, Q. Jiang, Adv. Funct. Mater. 29 (2019) 1901949.
[19] S. Zheng, X. Guo, H. Xue, et al., Chem. Commun. 55 (2019) 10904–10907.
[20] W. Xia, A. Mahmood, R. Zou, Q. Xu, Energy Environ. Sci. 8 (2015) 1837–1866.
[21] M. Zhang, Q. Dai, H. Zheng, M. Chen, L. Dai, Adv. Mater. 30 (2018) 1705431.
[22] L. Yang, X. Zeng, W. Wang, D. Cao, Adv. Funct. Mater. 28 (2018) 1704537.
[23] X. Li, X. Yang, H. Xue, H. Pang, Q. Xu, Energy Chem. 2 (2020) 100027.
[24] D. Zhu, Y. Huang, J.-j. Cao, et al., Appl. Catal. B 258 (2019) 117981.
[25] S. Dou, X. Li, L. Tao, J. Huo, S. Wang, Chem. Commun. 52 (2016) 9727–9730.
[26] Q. Wang, Y. Lei, Z. Chen, et al., J. Mater. Chem. A 6 (2018) 516–526.
[27] L. Zong, X. Chen, S. Dou, et al., Chin. Chem. Lett. 32 (2021) 1121–1126.
[28] P. Huang, H. Li, X. Huang, D. Chen, ACS Appl. Mater. Interfaces 9 (2017) 21083–21088.
[29] G. Panomsuwan, N. Saito, T. Ishizaki, ACS Appl. Mater. Interfaces 8 (2016) 6962–6971.
[30] Z. Xiao, G. Xiao, M. Shi, Y. Zhu, ACS Appl. Mater. Interfaces 10 (2018) 16436–16448.
[31] J. Xia, K. Jiang, J. Xie, et al., Chem. Eng. J. 359 (2019) 1244–1251.
[32] D. Ji, L. Fan, L. Li, et al., Adv. Mater. 31 (2019) 1808267.
[33] S. Surendran, S. Shanmugapriya, A. Sivanantham, R. Kalai Selvan, Adv. Energy Mater. 8 (2018)1800555.
[34] K. Zhou, B. Mousavi, Z. Luo, et al., J. Mater. Chem. A 5 (2017) 952–957.
[35] C. Wang, W. Chen, D. Yuan, et al., Nano Energy 69 (2020) 104453.
[36] L. Yu, B.Y. Xia, X. Wang, X.W. Lou, Adv. Mater. 28 (2016) 92–97.
[37] M. Huang, L. Wang, K. Pei, et al., Small 16 (2020) 2000158.
[38] T. Huang, Y. Chen, J.M. Lee, Small 13 (2017) 1702753.
[39] Y. Sun, S. Wang, J. Ning, et al., Nanoscale 12 (2020) 991–1001.
[40] B. Yin, X. Cao, A. Pan, et al., Adv. Sci. 5 (2018) 1800829.
[41] Q. Lu, J. Yu, X. Zou, et al., Adv. Funct. Mater. 29 (2019) 1904481.
[42] C.Y. Su, H. Cheng, W. Li, et al., Adv. Energy Mater. 7 (2017) 1602420.
[43] S. Wan, J. Wu, D. Wang, et al., Chin. Chem. Lett. 32 (2021) 816–821.
[44] H. Wang, Y. Yang, Q. Li, et al., Sci. China Mater. 64 (2021) 840–851.
[45] S. Zheng, Q. Li, H. Xue, H. Pang, Q. Xu, Nat. Sci. Rev. 7 (2020) 305–314.
[46] M. Zhang, M. Chen, Y. Bi, et al., J. Mater. Chem. A 7 (2019) 12893–12899.
[47] J. Bai, T. Meng, D. Guo, et al., ACS Appl. Mater. Interfaces 10 (2018) 1678–1689.
[48] Y.Y. Chen, Y. Zhang, W.J. Jiang, et al., ACS Nano 10 (2016) 8851–8860.
[49] W. Liu, J. Zhang, Z. Bai, et al., Adv. Funct. Mater. 28 (2018) 1706675.
[50] G. Fu, J. Wang, Y. Chen, et al., Adv. Energy Mater. 8 (2018) 1802263.
[51] Q. Mo, N. Chen, M. Deng, L. Yang, Q. Gao, ACS Appl. Mater. Interfaces 9 (2017) 37721–37730.
[52] F. Cao, G. Pan, Y. Zhang, X. Xia, Chin. Chem. Lett. 31 (2020) 2230–2234.
[53] H. Li, X. Qian, C. Xu, et al., ACS Appl. Mater. Interfaces 9 (2017) 28394–28405.
[54] X. Li, J. Wei, Q. Li, et al., Adv. Funct. Mater. 28 (2018) 1800886.
[55] L. Yan, H. Wang, J. Shen, et al., Chem. Eng. J. 403 (2021) 126385.
[56] Y. Li, L. Wang, J. Low, et al., Chin. Chem. Lett. 31 (2020) 231–234.
[57] E. Hu, J. Ning, D. Zhao, et al., Small 14 (2018) 1704233.